Open shells in endohedral clusters: structure and bonding in the $[Fe_2@Ge_{16}]^{4-}$ anion and comparison to isostructural $[Co_2@Ge_{16}]^{4-}$

Harry W. T. Morgan,[†] Katja-Sophia Csizi,[†] Ya-Shan Huang,[‡] Zhong-Ming Sun,[*,‡] and John E. McGrady[*,†]

[†]*Department of Chemistry, University of Oxford, South Parks Road, Oxford OX1 3QR, U.K.*

[‡]*Tianjin Key Lab of Rare Earth Materials and Applications, School of Materials Science and Engineering, Nankai University, Tianjin 300350, China*

E-mail: sunlab@nankai.edu.cn; john.mcgrady@chem.ox.ac.uk

Abstract

The anionic cluster $[Fe_2@Ge_{16}]^{4-}$ has been characterized and shown to be isostructural to the known D_{2h}-symmetric α isomer of the cobalt analogue, $[Co_2@Ge_{16}]^{4-}$. Together with the known pair of compounds $[Co@Ge_{10}]^{3-}$ and $[Fe@Ge_{10}]^{3-}$, the title compound completes a set of four closely-related germanium clusters that allow us to explore how the metal-metal and metal-cage interactions evolve as a function of size and of the identity of the metal. The results of spin-unrestricted Density Functional Theory (DFT) and Multi-Configurational Self-Consistent Field (MC-SCF) calculations present a consistent picture of the electronic structure where transfer of electron density from the metal to the cage is significant, particularly in the Fe clusters where the exchange stabilization of unpaired spin density is an important driving force.

Keywords

Endohedral clusters, X-ray crystallography, Density Functional Theory, CASSCF

Introduction

Over the past decade the electronic structure of clusters of main-group elements such as Si, Ge, Sn and Pb has been interrogated using the whole gamut of theoretical techniques. The majority of this work has been done using Density Functional Theory (DFT),[1–12] although the Complete Active Space Self Consistent Field (CASSCF) technique has also emerged in recent years as an important alternative.[13–20] Of particular interest to us has been how the properties of the cluster are modified by the presence of one or more endohedrally encapsulated transition metals, some of which are summarized in Figure 1. There has been a concerted effort to understand the growth mechanisms of these clusters,[21] with a view to establishing rational synthetic routes to ever higher nuclearities: some recent highlights from our own groups include the characterization of $[Rh_3@Sn_{24}]^{5-}$[22] and $[Au_{12}Pb_{44}]^{8-}$[23] in the solid state. These, along with the majority of other endohedral Zintl clusters, can be understood as closed-shell (d^{10}) transition metal ions encapsulated in an approximately deltahedral cage (by 'approximately deltahedral' we imply here a structure dominated by triangular faces).[2] In Eichhorn's $[Ni@Pb_{10}]^{2-}$ cluster shown in Figure 1, for example, the 52 valence electrons can be separated cleanly into 10 on the nickel (Ni^0) and 42 on the cluster, precisely the $4n+2$ count required for a *closo* deltahedron.[24]

There is, however, a small number of clusters containing transition metals from the middle of the first transition series (Mn and Fe) that present a rather different electronic landscape. In these cases a closed-shell d^{10} configuration would imply an unrealistically high formal negative charge on the metal center, and, perhaps unsurprisingly, their structural and electronic properties seem to be driven by transfer of electron density onto the tetrel cage rather than an accumulation of a closed electron shell at the metal. A case in point is the

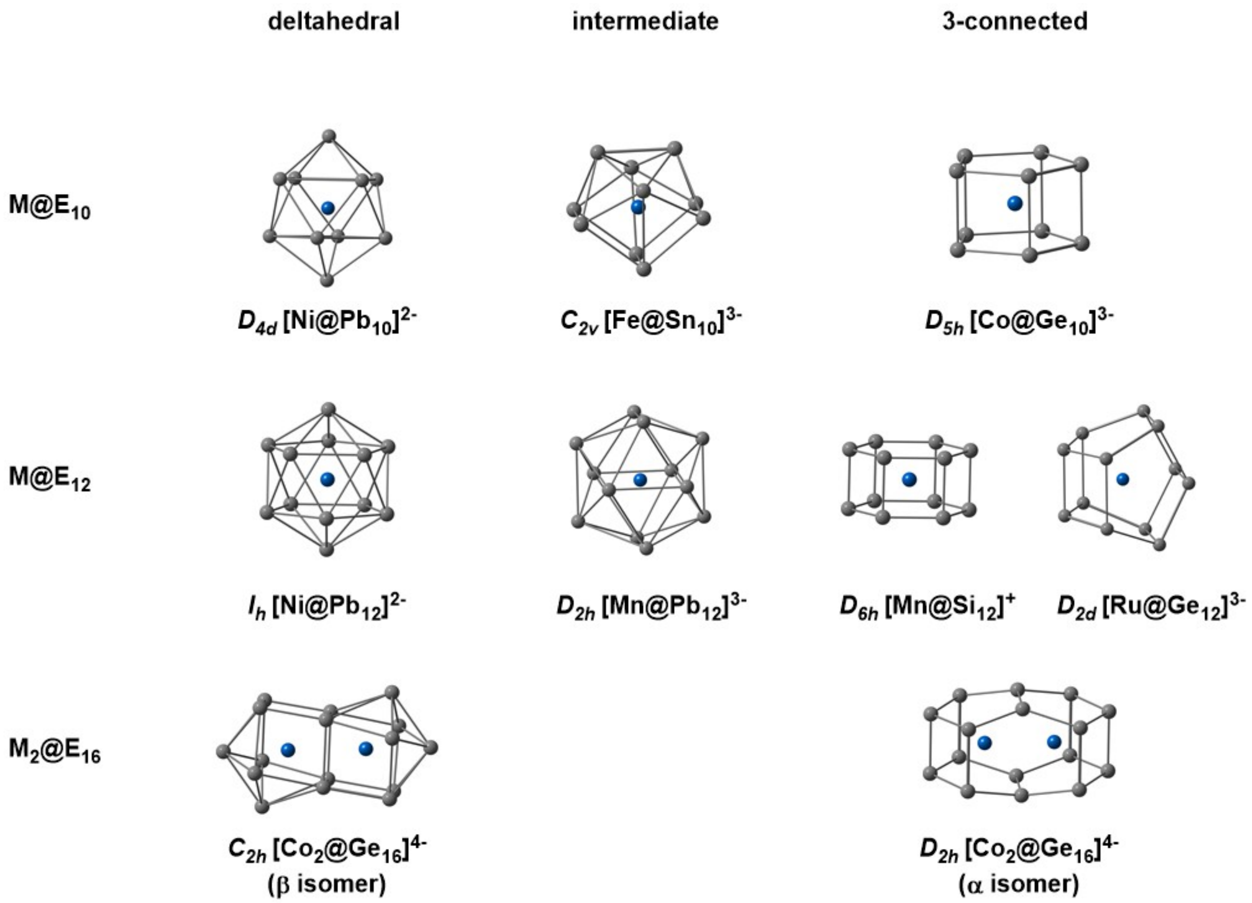

Figure 1: Structural types found in cluster types $M@E_{10}$, $M@E_{12}$ and $M_2@E_{16}$.[14,25–31]

highly distorted icosahedral $[Mn@Pb_{12}]^{3-}$ cluster reported by Goicoechea and co-workers in 2011,[29] where a closed-shell d^{10} configuration at Mn would imply a somewhat unrealistic formal -3 oxidation state. Instead, the transfer of spin-β electron density onto the cage allows spin-α density to accumulate on the Mn center, reducing electron-electron repulsion through exchange stabilization of the system. A more physically insightful formulation of the electron density distribution is therefore $[Mn^{2+}Pb_{12}{}^{5-}]$, a description that emphasises the presence of the incipient half-filled shell ($S = 5/2$, d^5) that would be realised at Mn in the limiting case that all spin-β $3d$ electrons are expelled from the metal. Despite the distortion, the geometry of $[Mn@Pb_{12}]^{3-}$ remains recognisably deltahedral, but a much more extreme case is found in the $[M@Ge_{10}]^{3-}$ clusters (M = Co, Fe),[27,32,33] where the structure is no longer deltahedral but pentagonal prismatic, based on square and pentagonal faces rather than triangles. Each vertex is therefore bonded to three others, and 'three-connected' structures of this type are commonly adopted by electron-precise clusters such as P_4 which have 5 valence electrons per vertex. The structural properties of the $[Co@Ge_{10}]^{3-}$ cluster appear, therefore, to be signalling the presence of 50 electrons on the Ge_{10} unit, but this presents a challenge for electron counting, because the total number of available valence electrons is only 52. If 50 of these are assigned to the Ge_{10} unit it leaves the metal centre with only 2 and a rather unphysical Co^{7+} oxidation state, while, conversely, if the Co $3d$ shell is assumed to be complete (Co^{-}), we have only 42 electrons on the cage, a number that seems inconsistent with the 3-connected structure. It is clear, therefore, that we cannot have mutually exclusive subsets of electrons that satisfy the valence requirements of the metal and the cage in the same way that we do for $[Ni@Pb_{10}]^{2-}$, despite the fact that the two clusters share a common valence-electron count of 52. In the language of Venn diagrams, there must be overlap, such that a subset of the electrons has a dual role, contributing simultaneously to the valence demands of the metal and of the cage. This idea is the essence of the 'jig-saw' model of cluster bonding which we have developed in recent papers,[1,2,34] and which we will explore further in subsequent sections. Whilst the number of compounds that fall into this 3-connected category remains small, examples such as $[Ru@Ge_{12}]^{3-}$, which adopts a D_{2d}-symmetric geometry, show that their occurrence is not restricted to the first transition series.[30] In 2015 and 2018, our two groups independently reported the 16-vertex cluster $[Co_2@Ge_{16}]^{4-}$. The initial report, by Goicochea and McGrady,[34] described its synthesis but all attempts to resolve the crystal structure were frustrated by disorder. DFT calculations reported in this paper did, however, offer some insights into the possible origin of the disorder by confirming that there are two almost iso-energetic isomers, one with D_{2h} symmetry that resembles two $Co@Ge_{10}$ pentagons fused *via* a square face and another with C_{2h} symmetry with predominantly triangular faces, typical of an approximately deltahedral architecture. In a subsequent paper, Sun and Boldyrev managed to resolve the disorder problem and confirmed that the compound crystallizes as a mixture of the two isomers that had been predicted to be close in energy, which they called α (D_{2h}) and β (C_{2h}), respectively.[31] Analysis of the electronic structure using the Adaptive Natural Density Partitioning (AdNDP) methodology confirmed profound differences in electronic structure between the two: whilst the α isomer can be described succinctly in terms of localized 2-center-2-electron bonds, the β isomer is better considered in terms of multi-center bonding typical of deltahedral clusters. The fascination with this cluster, therefore, is that it appears to sit right on the boundary between deltahedral and 3-connected clusters, leading to this remarkable example of structural isomerism. In this paper we begin with a report of the synthesis and structural characterization of the Fe analogue, $[\mathrm{Fe_2@Ge_{16}}]^{4-}$, which crystallizes exclusively in the α (D_{2h}-symmetric) form. The Fe cluster has two fewer electrons than the Co analogue so is manifestly less electron rich, but the lower effective nuclear charge means that the available metal-based electron density is less tightly bound to the metal centers, and therefore more able to interact with the orbitals on the cage. The switch from Co to Fe also takes us a step closer to the middle of the first transition series, where the effects of exchange stabilization will inevitably become more influential in differentiating majority- and minority-spin electrons. All of the above arguments mean that it is difficult to judge, *a priori*, how the distribution of charge between metal and cage will be influenced by the changing identity of the metal. With the structural characterization of $[\mathrm{Fe_2@Ge_{16}}]^{4-}$ that we report in the first section of the paper, we now have two pairs of Fe/Co clusters that are both isostructural and isovalent, containing either one ($[\mathrm{M@Ge_{10}}]^{3-}$) or two ($[\mathrm{M_2@Ge_{16}}]^{4-}$) transition metal centers. This quartet of clusters offers an opportunity to explore how changes in the identity of the metal can influence the nature of bonding, both between metals and between metal and cage. We employ both spin-unrestricted Kohn-Sham DFT and Multi-Configurational SCF (MC-SCF) methods to provide different but, ultimately, complementary perspectives on the electronic structure.

Methodology

Experimental Techniques

All operations were carried out under a nitrogen atmosphere using standard Schlenk or glovebox techniques. Ethylenediamine (Aldrich, 99%) and toluene (Aldrich, 99.8%) were freshly distilled over sodium and stored under nitrogen. [2.2.2]crypt (4,7,13,16,21,24-hexaoxa-1,10-diazabicyclo [8.8.8]hexacosane, was purchased from Sigma-Aldrich (98%) and dried under vacuum for 12 hours prior to use. The Zintl precursor phase "$KGe_{1.67}$" and the iron starting material, $[KFe(OtBu)_3]_2$, were prepared according to a previously reported synthetic procedures.[35,36] $KGe_{1.67}$ (80 mg, 0.5 mmol) and [2.2.2]crypt (90 mg, 0.238 mmol) were dissolved in ethylenediamine (2.5 mL) in a test tube inside a glovebox, producing a red solution. This solution was then stirred for 30 minutes before addition of $[KFe(OtBu)_3]_2$ (13 mg, 0.04 mmol). The dark brown reaction mixture was then stirred for a further hour, at which point it had turned into a brown suspension. The suspension was filtered and the resulting filtrate was layered with toluene to promote crystallization. Dark-red block crystals (shown in Supporting information, Figure S1) of $[K(2.2.2)\,crypt]_4[Fe_2@Ge_{16}]$ were obtained after two weeks in <5% yield based on the amount of $KGe_{1.67}$ used. Subsequent attempts to improve the yield by modifying the precursors or reaction conditions proved unsuccessful. Crystallographic data were collected on a Rigaku XtalAB Pro MM007 DW diffractometer with graphite monochromated Cu Kα radiation (λ = 1.54184Å). Structures were solved using direct methods and then refined using SHELXL-2014 and Olex2 to convergence,[37,38] where all the non-hydrogen atoms were refined anisotropically except for those in the split positions (see below). All hydrogen atoms of organic groups were placed using geometrical considerations. The disorder of the cluster anion over two orientations on the same site was incorporated into the model, with the best fit emerging for a ratio of 87:13 for the major/minor orientations. The internal structure of the anion is almost identical in the two orientations. Full details of the crystallography are given in the supporting information,

Table S1.

Computational Techniques

All DFT calculations were performed using the Amsterdam Density Functional (ADF) package, version 2019.304.[39] Slater-type basis sets of triple-zeta + polarization quality were used on all atoms, with orbitals up to 2p (Fe/Co) and 3d (Ge) included in the frozen core.[40] The Perdew-Becke-Ernzerhof (PBE)[41] functional was used in all calculations unless stated otherwise. The confining effect of the cation lattice was approximated using a continuum solvent model with a dielectric constant of 78.39. All calculations on Co complexes were performed using spin-restricted DFT while those for Fe clusters were spin-unrestricted (doublet and triplet ground states for $[Fe@Ge_{10}]^{3-}$ and $[Fe_2@Ge_{16}]^{4-}$, respectively). CASSCF and GASSCF calculations were performed using the OpenMolcas code,[42,43] pymolcas version py2.02, with an all-electron atomic natural orbital basis set. All CASSCF and GASSCF calculations were done using the optimized geometries obtained from the DFT calculations. Calculations on $[M@Ge_{10}]^{3-}$ used the D_{2h} subgroup rather than the full D_{5h} point symmetry, although results are labelled according to the latter. Calculations on $[M_2@Ge_{16}]^{4-}$ used the full D_{2h} molecular symmetry. The ANO basis for Co contains a 17s12p9d primitive set contracted to 5s4p2d, while for Ge a 17s15p9d primitive set is contracted to 5s4p1d (ANO-S-VDZ in the OpenMolcas library).[44]

Results and Discussion

Synthesis and structural characterization of $[K(2.2.2-crypt)]_4[Fe_2@Ge_{16}]$

$[K(2.2.2-crypt)]_4[Fe_2@Ge_{16}]$ was synthesized according to the procedures set out in the experimental section. Single-crystal X-ray diffraction reveals that the complex crystallizes in the triclinic space group P1 and that the asymmetric unit contains one crystallographically distinct $[Fe_2@Ge_{16}]^{4-}$ anion along with four $[K(2.2.2-crypt)]^+$ cations (Figure S3-4, CSD reference 2054930). Energy Dispersive X-ray spectroscopy (see Supporting information, Figure S4) confirms a molar ratio K/Fe/Ge of 3.8:1.9:16, close to the 4:2:16 ratio anticipated based on the crystal structure. The cluster anion shown in Figure 2 is disordered over two orientations, the major one having an occupation of 85.7% (Figure S2). The structural features of the two components are, however, almost identical so we restrict our discussion here to the major component. The cluster adopts the D_{2h}-symmetric structure of the α- isomer of $[Co_2@Ge_{16}]^{4-}$, with two endohedral Fe atoms inside a continuous 16-vertex 3-connected Ge cage which can also be viewed as the fusion of two pentagonal $[Fe@Ge_{10}]^{3-}$ units through a shared rectangular face. The most striking difference between $[Co_2@Ge_{16}]^{4-}$ and $[Fe_2@Ge_{16}]^{4-}$ is the distance between the metal atoms: 2.753(5) Å in the former[31] but only 2.636(3) Å in the latter. It is notoriously difficult to establish a direct correlation between bond length and bond order in complexes where bridging ligands may constrain the geometry even in the absence of direct bonding, but the Fe-Fe distance is certainly comparable to the value of 2.6869(6) Å in $Fetim_2$ (tim = 2,3,9,10-tetramethyl-1,4,8,11-tetraazacyclotetradeca-1,3,8,10-tetraene), where a bonding interaction between two Fe atoms is unambiguously present.[45] It is also shorter than those in typical dinuclear iron carbonyl complexes such as $[Fe_2(CO)_8]^{2-}$ (2.780(1)-2.815(1) Å),[46,47] $[(\eta_3\text{-}C_3H_5)Fe(CO)_3]_2$ (3.138(3) Å),[48] and $[Fe(CO_2tBu)(CO)_4]_2$ (2.840(1) Å).[49] Thus, in contrast to the α-$[Co_2@Ge_{16}]^{4-}$ case, $[Fe_2@Ge_{16}]^{4-}$ offers the possibility of direct Fe-Fe bonding. Apart from the differences in M-M bond distance, the structural metrics of the two clusters are otherwise remarkably similar. Compared to the $[M@Ge_{10}]^{3-}$ clusters, the M-Ge bonds in $[M_2@Ge_{16}]^{4-}$ are somewhat longer (2.578(3)-2.658(3) Å in $[Fe_2@Ge_{16}]^{4-}$ *vs* 2.5087(7)-2.5353(7) Å in $[Fe@Ge_{10}]^{3-}$, for example). Conversely the Ge-Ge bond lengths in $[Co_2@Ge_{16}]^{4-}$ (2.4933(8)-2.5922(9) Å) and $[Fe_2@Ge_{16}]^{4-}$ (2.506(2)-2.614(3) Å) are rather short in comparison to the majority of Ge clusters where values are typically greater than 2.60 Å.

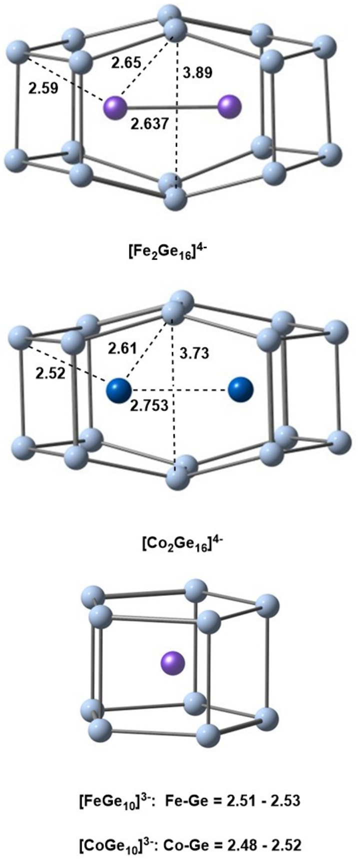

Figure 2: Key bond lengths (in Å) in the X-ray structure of $[Fe_2@Ge_{16}]^{4-}$ anion and comparison to isovalent $[Co_2@Ge_{16}]^{4-}$ and to $[M@Ge_{10}]^{3-}$, M = Co, Fe.[31]

Density Functional Theory

$[\mathbf{Co@Ge_{10}}]^{3-}$, $[\mathbf{Co_2@Ge_{16}}]^{4-}$ and the jigsaw bonding model.

The electronic structure of the $[M@Ge_{10}]^{3-}$ clusters has been discussed by a number of authors including ourselves,[9,26,27] but we show here how its structure can be understood at a qualitative level using the jigsaw model. The optimized structures of the two clusters, $[Fe@Ge_{10}]^{3-}$ and $[Co@Ge_{10}]^{3-}$, are unremarkable and fully consistent with experiment (shown in Supporting Information, Figure S5). The frontier Kohn-Sham molecular orbitals of the singlet ground state of $[Co@Ge_{10}]^{3-}$ are shown in Figure 3(a), alongside the density of states (DOS) obtained by Lorentzian broadening of the discrete levels. The DOS proves to be a particularly useful tool when comparing clusters of identical elemental composition but different structures and symmetries because it emphasises the broad trends in composition rather than focusing on individual orbitals, the shapes of which are necessarily dictated by symmetry. There are four pairs of electrons ($3e'_2$ and $3e''_1$ in Figure 3) involved in Co-Ge bonding and an additional pair of electrons in the $4a'_1$ orbital that is essentially Co-Ge non-bonding. The distinction between bonding and non-bonding levels is immediately apparent in the splitting of the Co $3d$ DOS in an approximately 4:1 ratio. How can we understand this structure in terms of the competing electronic demands of the metal and the cage, and in particular why the cage adopts a structure that appears to be consistent with an electron-precise (50-electron) count? The 50 electrons of a putative $[\mathrm{Ge}_{10}]^{10-}$ cage can be divided into 30 electrons in the 15 Ge-Ge single bonds and 20 in lone pairs that radiate outwards from each vertex. A symmetry analysis offers some important insights: the $3n/2$ (= 15) Ge-Ge bonding orbitals span $2\times a'_1 + 1\times a''_2 + 2\times e'_1 + 2\times e'_2 + 1\times e'_2 + 1\times e''_2$ while the n (= 10) radial lone pairs span $1\times a'_1 + 1\times a''_2 + 1\times e'_1 + 1\times e'_2 + 1\times e''_2 + 1\times e''_2$. The sum of these, $3\times a'_1 + 2\times a''_2 + 3\times e'_1 + 3\times e'_2 + 2\times e'_2 + 2\times e''_2$, supplemented by 2 additional electrons in the non-bonding $4a'_1$ orbital, is precisely the 52-electron configuration of $[\mathrm{Co@Ge}_{10}]^{3-}$. Consider the electronic structure now from the perspective of the metal. If the metal is to attain a stable $3d^{10}$ configuration, all 5 of its $3d$ orbitals, which transform as $a'_1 + e'_2 + e''_1$, must be occupied. The only way that the requirements of the cage and the metal can be satisfied simultaneously is therefore if four orbitals, spanning $e'_2 + e''_1$ irreducible representations, contribute to both the count at the cage and the count at the metal: these are precisely the $3e'_2$ and $3e''_1$ orbitals identified in Figure 3, and their Ge-Ge bonding character can be seen in the delocalization tails (picked out in the red circles in the Figure) that extend towards the centers of the Ge-Ge bonds, either between the pentagons ($3e'_2$) or within them ($3e''_1$). The key differences between the electron counting schemes in $[\mathrm{Ni@Pb}_{10}]^{2-}$ and $[\mathrm{Co@Ge}_{10}]^{3-}$ are summarized in Venn-diagram form in Scheme 1.

The D_{2h}-symmetric α-isomer of $[\mathrm{Co}_2\mathrm{@Ge}_{16}]^{4-}$ is clearly closely related to the pentagonal prismatic $[\mathrm{Co@Ge}_{10}]^{3-}$ - each Ge vertex is again connected to three others, and so it is

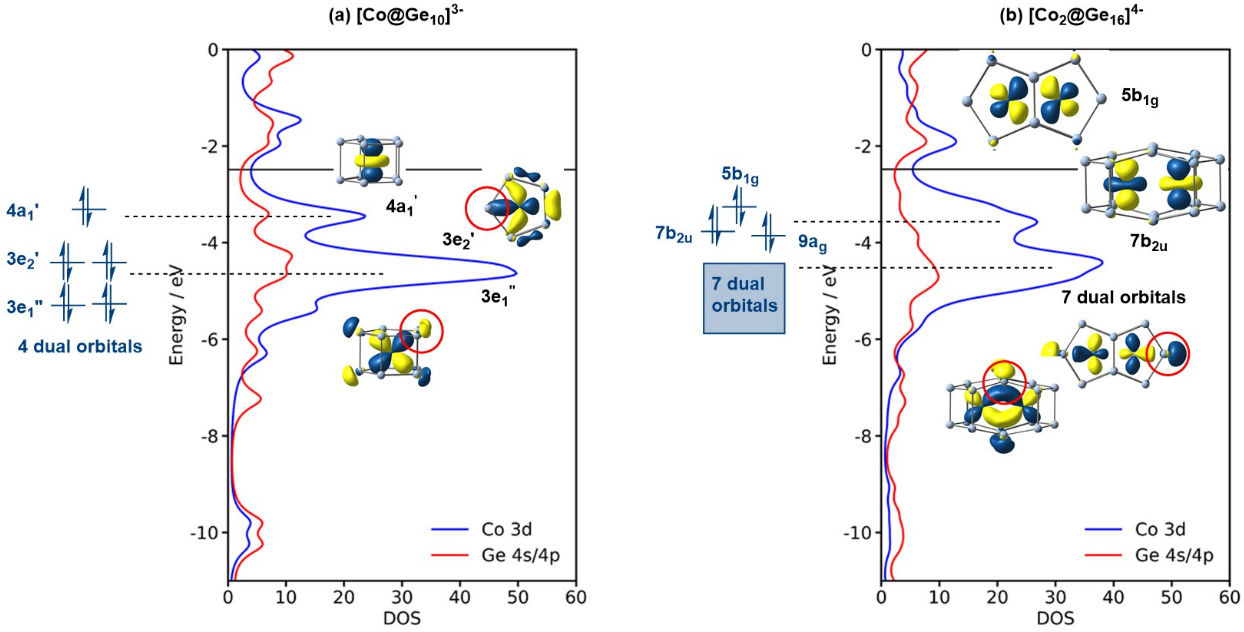

Figure 3: Densities of states and schematic molecular orbital diagrams for (a) $[Co@Ge_{10}]^{3-}$ and (b) $[Co_2@Ge_{16}]^{4-}$.

reasonable to ask whether the jigsaw model can also be applied to this rather more complex case with multiple transition metals. In contrast to clusters containing a single endohedral metal, where many theoretical studies have been reported, reports of the properties of clusters containing two or more metals, where the potential for metal-metal bonding introduces a new dimension to the problem, remain relatively scarce.[31,34,50–54] We can again make some progress by considering the problem from the perspective of electron count and symmetry. The total valence electron count for $[Co_2@Ge_{16}]^{4-}$ is 86, which separates into doubly oc-

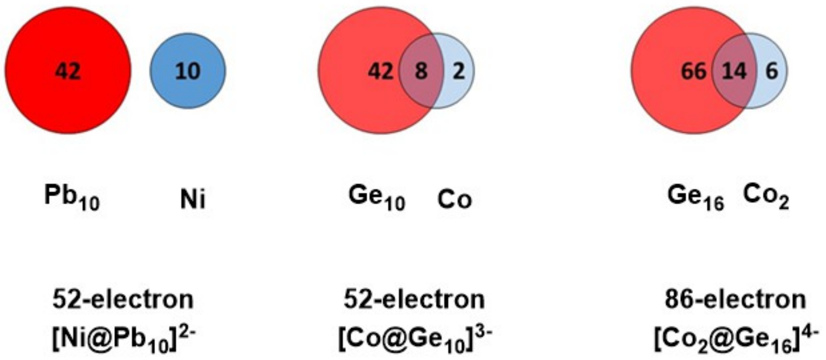

Scheme 1: Venn diagram representation of the jigsaw electron counting scheme.

cupied orbitals with $9 \times a_g + 5 \times b_{1g} + 4 \times b_{2g} + 4 \times b_{3g} + 3 \times a_u + 6 \times b_{1u} + 7 \times b_{2u} + 5 \times b_{3u}$ symmetry. The anticipated count for a 16-vertex, electron precise (3-connected), structure is $5n = 80$. By extension of the arguments made for $[\mathrm{Co@Ge_{10}}]^{3-}$, we should therefore expect the 86-electron count to separate into 33 doubly-occupied orbitals localized on the $\mathrm{Ge_{16}}$ cage, 7 double occupied orbitals with dual Co-Ge and Ge-Ge bonding character and 3 non-bonding orbitals localized on the metal centers. A symmetry analysis using the Ge-Ge bonds and radially-oriented lone pairs of the putative $[\mathrm{Ge_{16}}]^{16-}$ cluster as a basis (total dimension 40) gives $8 \times a_g + 4 \times b_{1g} + 4 \times b_{2g} + 4 \times b_{3g} + 3 \times a_u + 6 \times b_{1u} + 6 \times b_{2u} + 5 \times b_{3u}$. The difference between this and the total count, $a_g + b_{1g} + b_{2u}$ should, therefore, identify the symmetries of the three Co-Ge non-bonding orbitals, with the remaining 7 linear combinations with Co $3d$ character playing a dual role in precisely the same way that the $e_2' + e_1''$ orbitals did in $[\mathrm{Co@Ge_{10}}]^{3-}$. The DOS for $[\mathrm{Co_2@Ge_{16}}]^{4-}$ shown in Figure 3(b) is fully consistent with this model: the $3d$ band now splits in a 7:3 ratio with the upper region dominated by the three non-bonding orbitals, $9a_g$, $7b_{2u}$ and $5b_{1g}$. The $9a_g$ and $7b_{2u}$ orbitals are directed towards the centers of the pentagonal rings, and in that sense are the direct analogues of the d_{z^2} orbital in $[\mathrm{Co@Ge_{10}}]^{3-}$. The third non-bonding orbital, $5b_{1g}$, has Co-Co π^* character and is directed towards the elongated edges of the shared rectangular face linking the two pentagonal pyramids. In short, the detailed features of the valence orbitals of $[\mathrm{Co@Ge_{10}}]^{3-}$ and $[\mathrm{Co_2@Ge_{16}}]^{4-}$ show striking similarities, and both can be understood in terms of the jigsaw model where the available metal $3d$ density is partitioned into two energetically distinct subsets, one containing orbitals that contribute to both Co-Ge and Ge-Ge bonding (‘dual’ orbitals), and another containing orbitals that are strictly Co-Ge non-bonding and strongly localized on the transition metal centers.

Comparisons to paramagnetic $[\mathrm{Fe@Ge_{10}}]^{3-}$ and $[\mathrm{Fe_2@Ge_{16}}]^{4-}$.

The iron analogues, $[\mathrm{Fe@Ge_{10}}]^{3-}$ and $[\mathrm{Fe_2@Ge_{16}}]^{4-}$, differ from their cobalt analogues in having one and two fewer electrons, respectively. Superficially, we might anticipate that the removal of an electron from one of the non-bonding orbitals localized on the metals should have minimal impact on the strength of the M-Ge bonds, but as we illustrate below, the situation is somewhat more complex. The ground state of 51-electron $[\mathrm{Fe@Ge_{10}}]^{3-}$ is a doublet (Figure 4(a)), the singly occupied molecular orbital (SOMO) being the $4a_1'$ orbital which is, as noted above, localized almost exclusively on Fe d_{z^2}. The paramagnetic nature of the ground states splits the Kohn-Sham eigenvalues (and therefore the DOS) into separate spin-α and spin-β components but the 4:1 ratio between bonding and non-bonding levels is apparent in both sets. However, the different occupations of the a_1' orbital in $[\mathrm{Fe@Ge_{10}}]^{3-}$ and $[\mathrm{Co@Ge_{10}}]^{3-}$ has a significant impact on the electrons pairs in the $e_2' + e_1''$ orbitals that are involved in Co-Ge bonding. Evidence for this differential effect comes from the expectation value of $\langle S^2 \rangle = 0.84$, and the Mulliken spin densities, which show a distinct excess of spin-β density (-0.41 electrons) on the $\mathrm{Ge_{10}}$ cage and a corresponding excess of spin-α density (+1.41 electrons) on the Fe center: values for a simple Fe-based radical would be 0.0 and 1.0, respectively. The spin density plot shown at the bottom of Figure 4(a) illustrates the spatial resolution of the polarized electron density. The twin indicators, the deviation of $\langle S^2 \rangle$ from its ideal value of 0.75 and the presence of spin densities of opposite spin on the metal and the cage, are intimately linked, and are highly diagnostic of partial polarization of the electrons in the Co-Ge bonding orbitals ($3e_2'$ and $3e_1''$), such that the spin-β electrons are expelled outwards towards the cage while the spin-α electrons are drawn towards the metal where they are stabilized by the exchange interaction with the spin-α electron already present in the fifth $3d$ orbital. This 'seeding' of the polarization of the bonding density in the four e_2' and e_1'' orbitals by an unpaired electron in a non-bonding orbital is particularly pronounced in first row transition metals where the exchange interactions are most important, for example in $[\mathrm{Mn@Pb_{12}}]^{3-}$[29] and $[\mathrm{Mn@Si_{12}}]^{+}$.[14] We also note, in passing, that the degree of spin contamination, as measured by the deviation of $\langle S^2 \rangle$ from its idealized value, is strongly dependent on functional,and typical hybrids amplify the polarization. With the hybrid PBE0 functional,[55,56] for example, $\langle S^2 \rangle = 1.44$ and the spin densities are +2.33

and -1.33 on Fe and Ge_{10}, respectively. This extreme functional dependence has, in part, motivated the MC-SCF studies reported in the following section. Turning to $[Fe_2@Ge_{16}]^{4-}$, the first question to address relates to the structural isomerism: recall that $[Co_2@Ge_{16}]^{4-}$ crystallizes as a mixture of the α and β isomers in a disordered structure while only the α isomer is present in the crystal of $[Fe_2@Ge_{16}]^{4-}$. The computed energies of the two isomers for both Co and Fe suggest a thermodynamic origin for this trend: the α isomer is computed to be the more stable in both cases, but we find a distinct relative stabilization of the D_{2h}-symmetric isomer for Fe relative to Co ($\Delta E = E(D_{2h}) - E(C_{2h}) =$ -0.24 eV *vs* -0.17 eV). The optimized bond lengths for the α isomer of $[Fe_2@Ge_{16}]^{4-}$ are again in good agreement with experiment, with the ∼10% reduction in M-M separation for $[Fe_2@Ge_{16}]^{4-}$ faithfully reproduced (Supporting information, Figure S5).

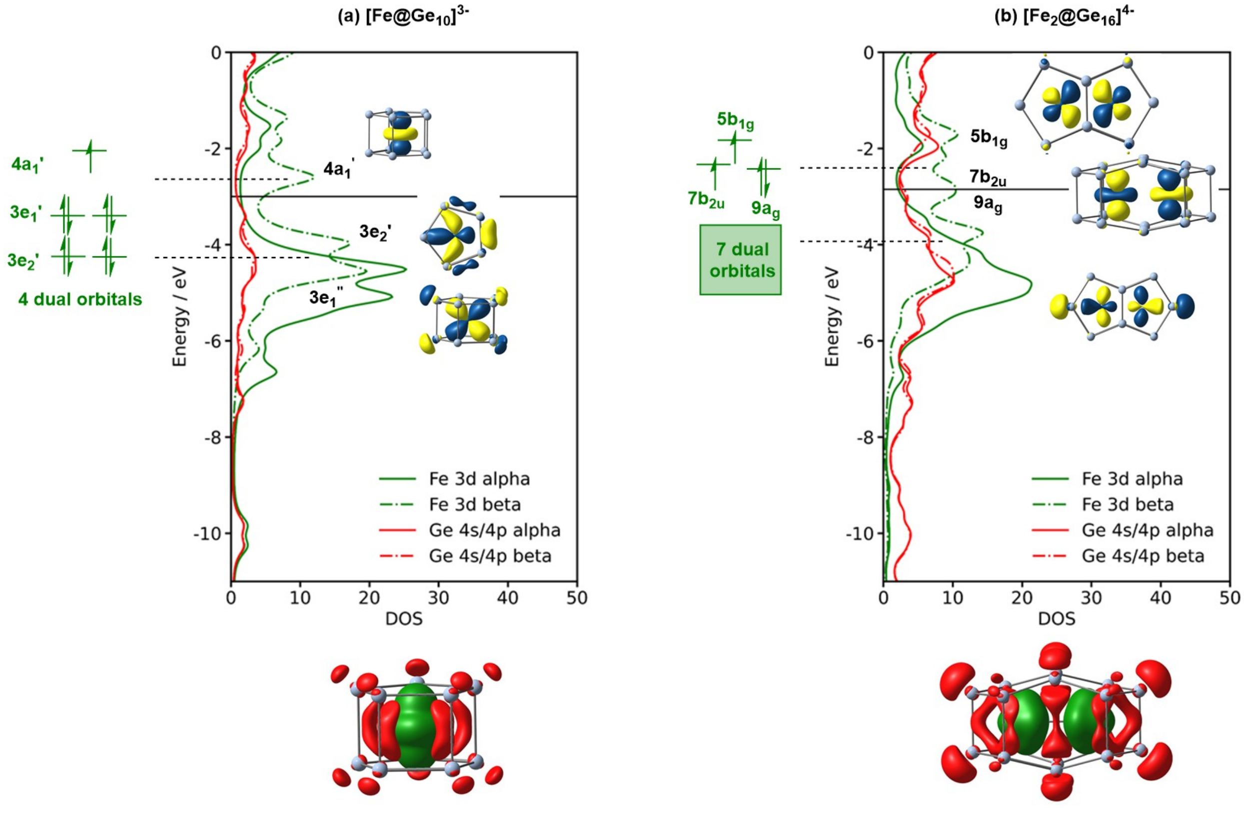

Figure 4: Densities of states (DOS), schematic molecular orbital diagrams and spin density plots for (a) $[Fe@Ge_{10}]^{3-}$ and (b) $[Fe_2@Ge_{16}]^{4-}$. In the spin density plots, regions of excess spin-α and spin-β densities are shown as green and red isosurfaces, respectively.

The computed ground state of $[\mathrm{Fe_2@Ge_{16}}]^{4-}$, with a total electron count of 84, is a triplet ($^3B_{3u}$) with vacancies in two of the three non-bonding orbitals, $7b_{2u}$ and $5b_{1g}$, identified above. In fact, the $^3B_{3u}$ state is the lowest of two closely spaced triplets, the other, $^3B_{1g}$, being generated by shifting a vacancy from the $7b_{2u}$ orbital to $9a_g$. The two states are qualitatively very similar in energy and electron distribution, so we dicuss only the most stable one in detail. The singly occupied $5b_{1g}$ orbital that is common to both triplets has distinct Fe-Fe π^* character while the $9a_g/7b_{2u}$ orbitals have δ or δ^* character, and make little contribution to Fe-Fe bonding. Based on this analysis we can assign a formal Fe-Fe bond order of $\sim$0.5 in both low-lying triplets. For reasons noted previously, it is extremely difficult to establish a direct connection between the metal-metal separation and the presence or absence of a metal-metal bond in the presence of bridging or, in this case, completely encapsulating, ligands. The Quantum Theory of Atoms in Molecules (QTAIM)[57] offers, at least in principle, an orbital-independent measure of Fe-Fe bond strength through an analysis of the topology of the electron density. The delocalization index (DI), a measure of the number of electron pairs delocalized over a pair of atoms, has been used with some success as a measure of bond order in transition metal chemistry.[58] For $[\mathrm{Co_2@Ge_{16}}]^{4-}$ and $[\mathrm{Fe_2@Ge_{16}}]^{4-}$, the DIs for the Fe-Fe and Co-Co pairs are 0.76 and 0.28, respectively, a clear indication of the emergence of significant Fe-Fe bonding in the latter. The strong spin polarization and spin contamination identified in $[\mathrm{Fe@Ge_{10}}]^{3-}$ is again apparent in the $^3B_{3u}$ ground state of $[\mathrm{Fe_2@Ge_{16}}]^{4-}$, where $\langle S^2 \rangle = 2.31$ compared to an ideal value of 2.0 for a pure triplet, and net spin densities on the $\mathrm{Fe_2}$ and $\mathrm{Ge_{16}}$ units are 2.99 and -0.99, respectively. The accumulation of excess spin-α density at each metal center, over and above that expected for a single unpaired electron, is therefore very similar in the two clusters, and the plots of spin densities in Figure 4(a) and (b) emphasise the strikingly similarities. This then points to a common underlying electronic structure, where the seeding of the polarization of the Fe-Ge bonding electron pairs by the presence of unpaired electrons in non-bonding orbitals maximizes exchange interactions between like-spin electrons.

Complete and Generalized Active Spaces, CASSCF and GASSCF

The very prominent spin contamination noted in the DFT calculations on both open-shell species, $[\mathrm{Fe@Ge_{10}}]^{3-}$ and $[\mathrm{Fe_2@Ge_{16}}]^{4-}$, typically goes hand-in-hand with substantial multi-configurational character in the corresponding *ab initio* wavefunction. To gain an alternative perspective on the electronic structure in this family of four clusters, we have therefore turned to MC-SCF calculations performed using the OpenMolcas code. As we will show, the $[\mathrm{M_2@Ge_{16}}]^{4-}$ clusters demand an extended active space that is beyond the limits of conventional CASSCF calculations, and so we make use of the Generalized Active Space (GAS) methodology, where correlating orbitals are separated into distinct groups, to eliminate configurations with close to zero weight from the CI expansion. The starting point for the MC-SCF study on the ${}^1A_1'$ ground state of $[\mathrm{Co@Ge_{10}}]^{3-}$ was a CAS(10,10) calculation, the active natural orbitals of which are shown in Figure 5 (the CAS(m,n) nomenclature indicates the presence of m electrons in n orbitals). The leading configurations for each of the states discussed in this section are collected in Table 1. The active space contains the two degenerate Co-Ge bonding orbitals, e_2' (d_{xy} and $d_{x^2-y^2}$) and e_1'' (d_{xz} and d_{yz}), along with their antibonding counterparts($e_2'^{*}$ and $e_1''^{*}$), and natural occupation numbers of 1.92/1.90 and 0.08/0.10, respectively, are indicative of significant multi-configurational character. The lead configuration, $e_1^{\prime\prime 4} e_1^{\prime\prime *0} e_2^{\prime 4} e_2^{\prime *0} a_1^{\prime 2} a_1^{\prime *0}$, makes up 83% of the wavefunction, with a number of smaller contributions that can be grouped according to double excitations of the following types: $e_1^{\prime\prime 2} e_1^{\prime\prime *2}$ (5%), $e_2^{\prime 2} e_2^{\prime *2}$ (3%) and $e_1^{\prime\prime 3} e_1^{\prime\prime *1} e_2^{\prime 3} e_2^{\prime *1}$ (5%). With an eye to the subsequent discussion of clusters containing two metals, we refer to this type of correlation between orbitals that are bonding/antibonding with respect to the metal/cage interaction as ‘in-out’ correlation. In their 2013 CASSCF study of $[\mathrm{Mn@Si_{14}}]^{+}$, Ngan and co-workers noted very similar in-out correlation in the Mn-Si bonds.[13] The fifth occupied Co 3d orbital, d_{z^2} (a_1'), has no antibonding partner and so correlates with a $4d_{z^2}$ orbital, a phenomenon usually described as the ‘double-shell’ effect. We have emphasized above the clear separation between the 8 Co-Ge bonding electrons (e_1'' and e_2') and the 2 non-bonding Co-based electrons (in a_1')

in the DOS, and the distinction is also reflected in the nature of the correlating orbitals in the MC-SCF wavefunction.

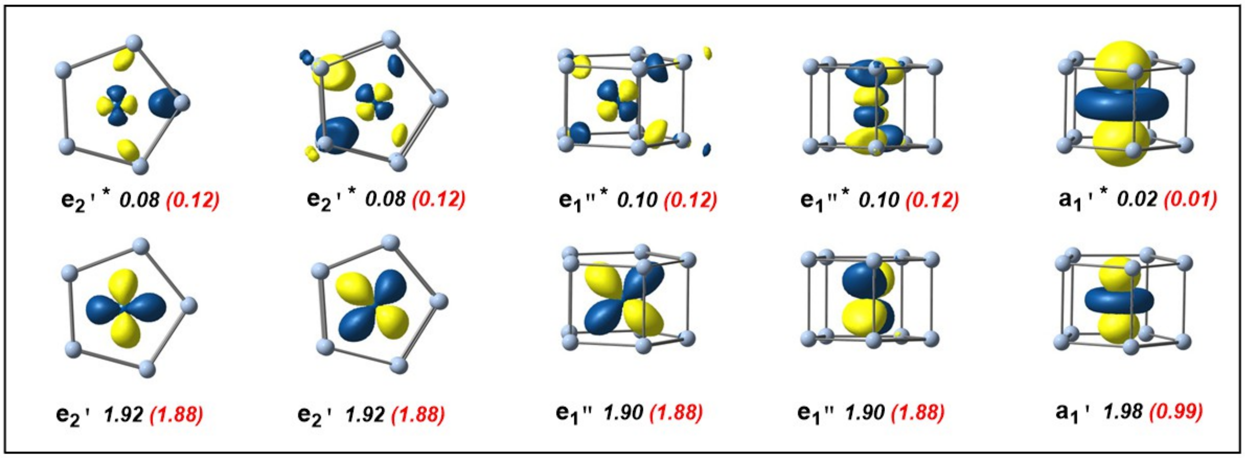

Figure 5: CAS(10,10) and CAS(9,10) active spaces for $[\mathrm{M@Ge_{10}}]^{3-}$. Natural occupations for Co are shown in back and the corresponding values for Fe in red. The orbitals shown are for Co but those for Fe are almost identical.

The ${}^2A_1'$ ground state of $[\mathrm{Fe@Ge_{10}}]^{3-}$ was described using a CAS(9,10) active space, and the lead configuration, $e_1''^4 e_1''^{*0} e_2'^4 e_2'^{*0} a_1'^1 a_1'^{*0}$, is identical to that for $[\mathrm{Co@Ge_{10}}]^{3-}$ save for the removal of a single electron from the a_1' orbital. The weight of the lead configuration is, however, reduced to 77% compared to 83% in $[\mathrm{Co@Ge_{10}}]^{3-}$ (Table 1) and small additional contributions to the wavefunction emerge from excitations of the $e_1''^3 e_1''^{*1}$ or $e_2'^3 e_2'^{*1}$ type, coupled to a spin-flip of the electron in the a_1' orbital (2% from each). The $e_1''^3 e_1''^{*1}$ and $e_2'^3 e_2'^{*1}$ excitations have zero weight in the wavefunction for closed-shell $[\mathrm{Co@Ge_{10}}]^{3-}$ because they would correspond to 1-electron excitations. The lower weight of the reference configuration leads to a reduction in the natural population numbers of the Co-Ge bonding orbitals (by ∼0.05) compared to the singlet ground state of $[\mathrm{Co@Ge_{10}}]^{3-}$, with concomitant increases in the occupation numbers of the antibonding orbitals. In short, the presence of a single unpaired electron, rather than an electron pair, in the a_1' orbital of $[\mathrm{Fe@Ge_{10}}]^{3-}$ increases the multi-configurational character of the wavefunction, reducing the effective bond order of the Fe-Ge bonds. It is important to emphasise that these differences in the MC-SCF wavefunction are driven by the same underlying physics as the strong spin contamination

Table 1: Leading Configurations in the CASSCF and GASSCF wavefunctions of the low-lying states of $[\mathrm{M@Ge}_{10}]^{3-}$ and $[\mathrm{M}_2\mathrm{@Ge}_{16}]^{4-}$. For the latter, orbitals are grouped in order GASa, GASb, GASc, GASd and GASe

	State	**Configuration**	**Weight(%)**
$[\mathrm{Co@Ge}_{10}]^{3-}$	$^1A_1'$	$e_1^{\prime\prime 4}e_1^{\prime\prime *0}e_2^{\prime 4}e_2^{\prime *0}a_1^{\prime 2}a_1^{\prime *0}$	83
		$e_1^{\prime\prime 2}e_1^{\prime\prime *2}e_2^{\prime 4}e_2^{\prime *0}a_1^{\prime 2}a_1^{\prime *0}$	5
		$e_1^{\prime\prime 4}e_1^{\prime\prime *0}e_2^{\prime 2}e_2^{\prime *2}a_1^{\prime 2}a_1^{\prime *0}$	3
		$e_1^{\prime\prime 3}e_1^{\prime\prime *1}e_2^{\prime 3}e_2^{\prime *1}a_1^{\prime 2}a_1^{\prime *0}$	5
$[\mathrm{Fe@Ge}_{10}]^{3-}$	$^2A_1'$	$e_1^{\prime\prime 4}e_1^{\prime\prime *0}e_2^{\prime 4}e_2^{\prime *0}a_1^{\prime 1}a_1^{\prime *0}$	77
		$e_1^{\prime\prime 2}e_1^{\prime\prime *2}e_2^{\prime 4}e_2^{\prime *0}a_1^{\prime 1}a_1^{\prime *0}$	4
		$e_1^{\prime\prime 4}e_1^{\prime\prime *0}e_2^{\prime 2}e_2^{\prime *2}a_1^{\prime 1}a_1^{\prime *0}$	4
		$e_1^{\prime\prime 3}e_1^{\prime\prime *1}e_2^{\prime 3}e_2^{\prime *1}a_1^{\prime 1}a_1^{\prime *0}$	5
		$e_1^{\prime\prime 3}e_1^{\prime\prime *1}e_2^{\prime 4}e_2^{\prime *0}a_1^{\prime 1}a_1^{\prime *0}$	2
		$e_1^{\prime\prime 4}e_1^{\prime\prime *0}e_2^{\prime 3}e_2^{\prime *0}a_1^{\prime 1}a_1^{\prime *0}$	2
$[\mathrm{Co}_2\mathrm{@Ge}_{16}]^{4-}$	^1A_g	$[b_{1u}^2b_{1u}^{*0}b_{3g}^2b_{3g}^{*0}][b_{2g}^2b_{2g}^{*0}a_u^2a_u^{*0}][a_g^2a_g^{*0}b_{3u}^2b_{3u}^{*0}][b_{2u}^2b_{2u}^{*0}b_{1g}^2b_{1g}^{*0}][a_g^2b_{3u}^2b_{3u}^{*0}]$	64
$[\mathrm{Fe}_2\mathrm{@Ge}_{16}]^{4-}$	$^3B_{3u}$	$[b_{1u}^2b_{1u}^{*0}b_{3g}^2b_{3g}^{*0}][b_{2g}^2b_{2g}^{*0}a_u^2a_u^{*0}][a_g^2a_g^{*0}b_{3u}^2b_{3u}^{*0}][b_{2u}^2b_{2u}^{*0}b_{1g}^1][a_g^2b_{3u}^1]$	42
	$^3B_{1g}$	$[b_{1u}^2b_{1u}^{*0}b_{3g}^2b_{3g}^{*0}][b_{2g}^2b_{2g}^{*0}a_u^2a_u^{*0}][a_g^2a_g^{*0}b_{3u}^2b_{3u}^{*0}][b_{2u}^2b_{2u}^{*0}b_{1g}^1][a_g^1b_{3u}^2]$	42

noted in the unrestricted Kohn-Sham calculations - the stabilizing exchange interactions associated with the half-filled d^5 shell. Thus we see the same ‘seeding’ phenomenon, reflected now in an MC-SCF context by enhanced multi-configurational character, rather than the spin contamination characteristic of UKS DFT.

Whilst the CAS(10,10) wavefunctions described in the previous paragraph do not present any problems in terms of dimensions of the active space, doubling the size to CAS(20,20) to accommodate the two metal centers in $[\mathrm{M}_2\mathrm{@Ge}_{16}]^{4-}$ would be beyond the limits of a conventional active space. The Generalized Active Space (GAS) approach partitions the active space into sub-groups, with either limited or no excitations allowed between the groups, thereby eliminating a large number of configurations which, if the GAS partitions are chosen appropriately, would make negligible contributions to the original CASSCF configuration interaction (CI) expansion.[59–62] As the GAS methodology will be critical in the subsequent section on $[\mathrm{M_2Ge_{16}}]^{4-}$, it is important to explore its performance in the simpler $[\mathrm{M@Ge_{10}}]^{3-}$ cases where the CAS(10,10) wavefunction is available as a benchmark. We have tested two separate GAS partitions, GAS3(10,10) and GAS5(10,10) where in the GASi(m,n) nomenclature, i indicates the number of GAS partitions while m and n again define the total number of electrons and orbitals, respectively, in the active space. In the GAS3(10,10) calculation the three separate partitions contain (i) 4 electrons in the 4 orbitals of e_2' symmetry (bonding and antibonding combinations of d_{xy}, $d_{x^2-y^2}$ with the cage) (ii) 4 electrons in the 4 orbitals of e_1'' symmetry (bonding and antibonding combinations of d_{xz}, d_{yz} with the cage) and (iii) 2 electrons in 2 orbitals of a_1' symmetry ($3d_{z^2}$ and its $4d$ double-shell counterpart). No excitations between the partitions were allowed. We can go a step further and separate out the degenerate components of the e_1'' and e_2' sets to generate a GAS5(10,10) space where each partition contains 2 electrons and 2 orbitals, again with no excitations allowed between the partitions. This type of extreme GAS partition has been called the 'separated pair' (SP) approximation.[62] The step from CAS(10,10) to GAS3(10,10) and then to GAS5(10,10) reduces the number of configuration state functions (CSFs) from 4956 to 1390 to 654, but the MC-SCF energy changes by less than 10^{-2} Hartree while the natural occupation numbers of the active orbitals change by less than 0.01. These observations confirm that the eliminated CSFs did indeed have close to zero weight in the original CAS(10,10) expansion. Thus a judicious choice of GAS partition in these high-symmetry systems can reduce the number of CSFs by almost an order of magnitude without significant deterioration in the quality of the CI wavefunction.

Turning now to the larger $[\mathrm{M_2@Ge_{16}}]^{4-}$ clusters, the presence of two transition metal atoms admits the possibility of 'left-right' correlation, alongside the 'in-out' correlation between metal and Ge cage discussed in the previous section, and this leads to a rather complex wavefunction where multi-determinantal character is more prevalent. The dominant 'in-out' (*i.e.* M-Ge) correlation pathways in $[\mathrm{M@Ge_{10}}]^{3-}$ proved to be between orbitals of e_2' ($d_{xy}/d_{x^2-y^2}$) symmetry and between orbitals of e_1'' symmetry (d_{xz} and d_{yz}). Collecting linear combinations of each of these four atomic components into separate active spaces (labelled GASa-d in Figure 6), generates a GAS4(16,16) wavefunction with 606822 CSFs. Including the two remaining occupied orbitals, a_{1g} and b_{3u} and their $4d$ counterparts would lead to a GAS5(20,20) wavefunction with $> 10^7$ configuration space functions, which is beyond the capacity of available resources. It did, however, prove possible to stabilize the two occupied d_{z^2} orbitals in the active space with only a single double-shell orbital (in GASe), leading, finally, to a GAS5(20,19) wavefunction (7267363 CSFs), the natural orbitals of which are shown in Figure 6.

Within each of each of the first three GAS spaces (GASa-c in Figure 6), each with 4 electrons in 4 orbitals, the nature and degree of correlation is broadly similar to that identified in $[\mathrm{Co@Ge_{10}}]^{3-}$. The dominant 2-electron excitations are again between orbitals that differ in bonding character with respect to Co-Ge interactions, but now also with respect to Co-Co character. These can be categorized as both 'in-out' and 'left-right' correlations. Taking GASb as an example, the double excitation from the b_{2g} orbital (Co-Co and Co-Ge bonding) to a_u^* (Co-Co antibonding and Co-Ge antibonding) has a coefficient of 1.5% in the final wavefunction compared to 64% for the Hartree-Fock configuration. There are, however, also non-negligible contributions from excitations that represent 'in-out' but not 'left-right' correlation: taking GASb as an example again, the b_{2g} to b_{2g}^* and a_u to a_u^* double excitations have coefficients of 0.8% and 0.6%, respectively. The similar weights of left-right and in-out correlation frustrates any attempts to further reduce the length of the CI expansion increasing the number of GAS partitions to 10 (*i.e.* the separated-pair approximation). Moving to GASe, which contains the linear combinations of d_{z^2} orbitals, we again note the

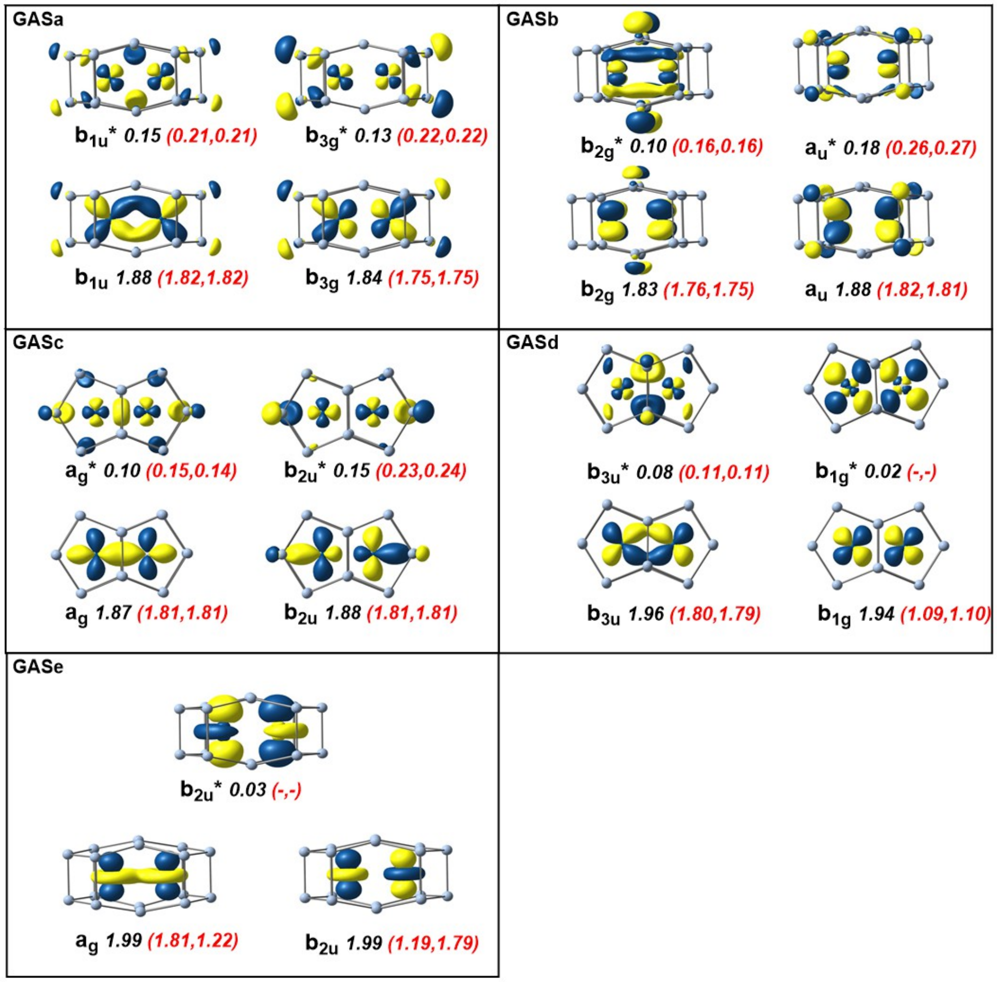

Figure 6: Natural orbitals and occupation numbers for the GAS5(20,19) active space of $[Co_2@Ge_{16}]^{4-}$ ($^1A_{1g}$ state) and the GAS5(18,17) active space of $[Fe_2@Ge_{16}]^{4-}$. Occupations for the Co cluster are shown in black, while the two numbers in red correspond to the $^3B_{3u}$ and $^3B_{1g}$ states of the Fe analogue. The orbitals shown are those for Co.

relationship to $[Co@Ge_{10}]^{3-}$ in so much as correlation from the $4d$ double shell is present but weak. The differences between $[Co@Ge_{10}]^{3-}$ and $[Co_2@Ge_{16}]^{4-}$ are most apparent in GASd, which contains the linear combinations of the atomic d_{xy} orbitals including the Co-Co $\pi*$ orbital of b_{1g} symmetry which we have identified as being one of the three non-bonding orbitals, and as a result the weakly occupied b_{1g}^* orbital is from the $4d$ set rather than a Co-Ge antibonding orbital.

In the $[Fe_2@Ge_{16}]^{4-}$ cluster, the lower electron count leads to an increase in the number of CSFs, so we have found it necessary to remove the two $4d$ double-shell correlating orbitals (b_{1g}^*

in GASd and b_{2u}^{*} in GASe), leaving a GAS5(18,17) wavefunction. Precisely as we reported in the DFT section, there are two low-lying triplet states, ${}^{3}B_{3u}$ and ${}^{3}B_{1g}$, both of which have a singly-occupied b_{1g} orbital in GASd in the lead configuration, along with another in GASe (either a_g or b_{2u} in ${}^{3}B_{1g}$ or ${}^{3}B_{3u}$, respectively). In the absence of a treatment of dynamic correlation we make no attempt to evaluate the relative energies of these states using MC-SCF theory: our discussion will focus on the ${}^{3}B_{3u}$ state identified as the ground state by DFT, but the patterns are qualitatively similar for both triplets (see Table 1) and Figure 6. The natural occupations of the active orbitals in GASa-c of the GAS5(18,17) space are qualitatively very similar to those for the GAS5(20,19) space for $[\mathrm{Co_2@Ge_{16}}]^{4-}$. The large number of excited configurations that make small but approximately equal contributions to the wavefunction preclude a detailed analysis such as that presented for $[\mathrm{Co@Ge_{10}}]^{3-}$ and $[\mathrm{Fe@Ge_{10}}]^{3-}$, but the deviations of the population numbers of the natural orbitals from 2.0 and 0.0 are again more pronounced in $[\mathrm{Fe_2@Ge_{16}}]^{4-}$ than in $[\mathrm{Co_2@Ge_{16}}]^{4-}$ (compare the black and red numbers in Figure 6), indicating an increase in 'in-out' correlation in the open-shell cluster. The strong seeding effect of the unpaired electrons localized on the metal centers clearly persists into the larger clusters. The picture of Fe-Fe bonding that emerges from the MC-SCF calculation is also broadly consistent with that from DFT. The occupation numbers in Figure 6 give an effective bond order (EBO) of 0.66 (defined as $\sum(\eta_b - \eta_a)/2$, where $\eta_{b/a}$ are the natural occupation numbers of orbitals that are Fe-Fe bonding or antibonding, respectively).[63] The dominant component of the total EBO comes from GASd (Fe-Fe π), which contributes an EBO_{π} of 0.41. There is a smaller δ component, $\mathrm{EBO}_{\delta} = 0.31$, in GASe but the overlap of the Fe-based orbitals in this case is very marginal.

Summary and conclusions

In this contribution we began by describing the synthesis and structure of the $[\mathrm{Fe_2@Ge_{16}}]^{4-}$ anion, which completes the quartet of structurally characterized endohedral germanium clusters, $[M@Ge_{10}]^{3-}$ and $[M_2@Ge_{16}]^{4-}$, M = Fe, Co. It is rare to have a complete set of binary clusters containing the same two elements that offers comparisons between neighboring transition metals and between clusters of different size. In this particular case, the lower electron count of the Fe clusters leads to paramagnetism in both $[Fe@Ge_{10}]^{3-}$ and $[Fe_2@Ge_{16}]^{4-}$. Perhaps counterintuitively, the lower electron count at Fe does not withdraw electron density from the cluster towards the metal - spin-β density is in fact expelled from the Fe_2 core onto the Ge_{16} cage, stabilizing the metal-based density through the strong exchange interactions that dominate much of the chemistry of the first transition series. The subtle changes in electronic structure between Co and Fe can be traced through spin-unrestricted Kohn-Sham DFT, where the key diagnostics are the spin contamination (as measured by $\langle S^2 \rangle$) and the Mulliken spin densities, and through MC-SCF theory, where the metric of interest is the degree of multi-configurational character. The MC-SCF approach is more nuanced, in the sense that the natural population numbers indicate a progressive increase in multi-configurational character from Co to Fe. The unrestricted Kohn-Sham approach, in contrast, is more black and white in that it does not identify any spontaneous symmetry breaking in $[Co@Ge_{10}]^{3-}$ so we have no indication of multi-configurational character in this case, other than that it is less prevalent than in $[Fe@Ge_{10}]^{3-}$. Notwithstanding these differences, the patterns identified using these two fundamentally different approaches to electronic structure are reflecting the same underlying phenomenon, which is that the stability of the half-filled $3d^5$ subshell is a dominant driving force in the electronic structure of mid-first row transition elements.

Acknowledgement

The synthetic aspects of this work were supported by the National Natural Science Foundation of China (21971118). HWTM thanks the EPSRC for support through the Centre for Doctoral Training, Theory and Modelling in Chemical Sciences, under grant EP/L015722/1, and the Radcliffe scholarship fund at University College, Oxford.

Supporting Information Available

Details of the X-ray diffraction experiment for $[Fe_2@Ge_{16}]^{4-}$ (Figures S1-3 and Table S1). Energy Dispersive X-ray (EDX) Spectroscopy (Figure S4 and Table S2). Optimized bond lengths for the clusters discussed here (Figure S5). A zip file containing optimized cartesian coorinates for all structures is also provided.

References

(1) Jin, X.; Arcisauskaite, V.; McGrady, J. E. The structural landscape in 14-vertex clusters of silicon, $M@Si_{14}$: when two bonding paradigms collide. *Dalton Trans.* **2017**, *46*, 11636–11644.

(2) Goicoechea, J. M.; McGrady, J. E. On the structural landscape in endohedral silicon and germanium clusters, $M@Si_{12}$ and $M@Ge_{12}$. *Dalton Trans.* **2015**, *44*, 6755–6766.

(3) Jin, X.; McGrady, J. E. In *Computational Chemistry*; van Eldik, R., Puchta, R., Eds.; Adv. Inorg. Chem.; Academic Press, 2019; Vol. 73; pp 265–304.

(4) Bandyopadhyay, D.; Sen, P. Density functional investigation of structure and stability of Ge_n and Ge_nNi (n = 1–20) clusters: validity of the electron counting rule. *J. Phys. Chem. A* **2010**, *114*, 1835–1842.

(5) Dhaka, K.; Bandyopadhyay, D. Study of the electronic structure, stability and magnetic quenching of $CrGe_n$ (n = 1–17) clusters: a density functional investigation. *RSC Adv.* **2015**, *5*, 83004–83012.

(6) He, J.; Wu, K.; Liu, C.; Sa, R. Stabilities of 3d transition-metal doped Si_{14} clusters. *J. Chem. Phys.* **2009**, *483*, 30–34.

(7) Chauhan, V.; Abreu, M. B.; Reber, A. C.; Khanna, S. N. Geometry controls the stability of $FeSi_{14}$. *Phys. Chem. Chem. Phys.* **2015**, *17*, 15718–15724.

(8) Ulises Reveles, J.; Khanna, S. N. Electronic counting rules for the stability of metal-silicon clusters. *Phys. Rev. B* **2006**, *74*, 035435.

(9) Uţă, M. M.; Cioloboc, D.; King, R. B. Cobalt-centered ten-vertex germanium clusters: the pentagonal prism as an alternative to polyhedra predicted by the Wade–Mingos rules. *Inorg. Chem.* **2012**, *51*, 3498–3504.

(10) Koukaras, E. N.; Garoufalis, C. S.; Zdetsis, A. D. Structure and properties of the Ni@Si_{12} cluster from all-electron ab initio calculations. *Phys. Rev. B* **2006**, *73*, 235417.

(11) Kumar, V.; Kawazoe, Y. Magic behavior of $Si_{15}M$ and $Si_{16}M$ (M = Cr, Mo, and W) clusters. *Phys. Rev. B* **2002**, *65*, 073404.

(12) Zhao, J.; Du, Q.; Zhou, S.; Kumar, V. Endohedrally doped cage clusters. *Chem. Rev.* **2020**, *120*, 9021–9163.

(13) Ngan, V. T.; Pierloot, K.; Nguyen, M. T. Mn@$Si_{14}{}^{+}$: a singlet fullerene-like endohedrally doped silicon cluster. *Phys. Chem. Chem. Phys.* **2013**, *15*, 5493–5498.

(14) Arcisauskaite, V.; Fijan, D.; Spivak, M.; Graaf, C. d.; McGrady, J. E. Biradical character in the ground state of $[Mn@Si_{12}]^{+}$: a DFT and CASPT2 study. *Phys. Chem. Chem. Phys.* **2016**, *18*, 24006–24014.

(15) Nguyen, M. T.; Tran, Q. T.; Tran, V. T. The ground and excited low-lying states of $VSi_2{}^{0/-/+}$ clusters from CASSCF/CASPT2 calculations. *Chem. Phys, Lett.* **2019**, *721*, 111–116.

(16) Tran, V. T.; Tran, X. M. T.; Nguyen, M. T.; Nguyen, H. T.; Tran, Q. T. A new interpretation of the photoelectron spectrum of $VSi_4{}^{-}$ cluster by density functional theory and multiconfigurational CASSCF/CASPT2 calculations. *Chem. Phys. Lett.* **2017**, *690*, 140–146.

(17) Tran, V. T.; Tran, Q. T. Low-lying electronic states of $\mathrm{FeGe}_n{}^{-/0}$ (n = 1–3) clusters calculated with multireference second-order perturbation theory. *J. Phys. Chem. A* **2020**, *124*, 4095–4105.

(18) Tran, V. T.; Tran, Q. T. The electronic structures of $\mathrm{CoGe}_n{}^{-/0}$ (n = 1–3) clusters from multiconfigurational CASSCF/CASPT2 and RASSCF/RASPT2 calculations. *J. Phys. Chem. A* **2018**, *122*, 6407–6415.

(19) Tran, V. T.; Nguyen, M. T.; Tran, Q. T. Computational investigation of the geometrical and electronic structures of $\mathrm{VGe}_n{}^{-/0}$ (n = 1–4) clusters by density functional theory and multiconfigurational CASSCF/CASPT2 method. *J. Phys. Chem. A* **2017**, *121*, 7787–7796.

(20) Tran, V. T.; Tran, Q. T. A density matrix renormalization group investigation on the electronic states of $\mathrm{MnGe}_n{}^{-/0/+}$ (n = 1–3) clusters. *International Journal of Quantum Chemistry* e26619.

(21) Mitzinger, S.; Broeckaert, L.; Massa, W.; Weigend, F.; Dehnen, S. Understanding of multimetallic cluster growth. *Nature Communications* **2016**, *7*, 10480.

(22) Liu, C.; Jin, X.; Li, L.-J.; Xu, J.; McGrady, J. E.; Sun, Z.-M. Synthesis and structure of a family of rhodium polystannide clusters $[\mathrm{Rh@Sn_{10}}]^{3-}$, $[\mathrm{Rh@Sn_{12}}]^{3-}$, $[\mathrm{Rh_2@Sn_{17}}]^{6-}$ and the first triply-fused stannide, $[\mathrm{Rh_3@Sn_{24}}]^{5-}$. *Chem. Sci.* **2019**, *10*, 4394–4401.

(23) Shu, C.-C.; Morgan, H. W. T.; Qiao, L.; McGrady, J. E.; Sun, Z.-M. A family of lead clusters with precious metal cores. *Nature Communications* **2020**, *11*, 3477.

(24) Wade, K. The structural significance of the number of skeletal bonding electron-pairs in carboranes, the higher boranes and borane anions, and various transition-metal carbonyl cluster compounds. *J. Chem. Soc. D* **1971**, 792–793.

(25) Esenturk, E. N.; Fettinger, J.; Eichhorn, B. The closo-${Pb_{10}}^{2-}$ Zintl ion in the $[Ni@Pb_{10}]^{2-}$ cluster. *Chem. Commun.* **2005**, 247–249.

(26) Krämer, T.; Duckworth, J. C. A.; Ingram, M. D.; Zhou, B.; McGrady, J. E.; Goicoechea, J. M. Structural trends in ten-vertex endohedral clusters, $M@E_{10}$ and the synthesis of a new member of the family, $[]Fe@Sn_{10}]^{-/0/+}$. *Dalton Trans.* **2013**, *42*, 12120–12129.

(27) Wang, J.-Q.; Stegmaier, S.; Fässler, T. $[Co@Ge_{10}]^{3-}$: an intermetalloid cluster with Archimedean pentagonal prismatic structure. *Angew. Chem., Int. Ed.* **2009**, *48*, 1998–2002.

(28) Esenturk, E. N.; Fettinger, J.; Eichhorn, B. The ${Pb_{12}}^{2-}$ and ${Pb_{10}}^{2-}$ Zintl Ions and the $M@{Pb_{12}}^{2-}$ and $M@{Pb_{10}}^{2-}$ cluster series where M = Ni, Pd, Pt. *J. Am. Chem. Soc.* **2006**, *128*, 9178–9186.

(29) Zhou, B.; Krämer, T.; Thompson, A. L.; McGrady, J. E.; Goicoechea, J. M. A highly distorted open-shell endohedral Zintl cluster: $[Mn@Pb_{12}]^{3-}$. *Inorg. Chem.* **2011**, *50*, 8028–8037.

(30) Espinoza-Quintero, G.; Duckworth, J. C. A.; Myers, W. K.; McGrady, J. E.; Goicoechea, J. M. Synthesis and characterization of $[Ru@Ge_{12}]^{3-}$: an endohedral 3-connected cluster. *J. Am. Chem. Soc.* **2014**, *136*, 1210–1213.

(31) Liu, C.; Popov, I. A.; Li, L.-J.; Li, N.; Boldyrev, A. I.; Sun, Z.-M. $[Co_2@Ge_{16}]^{4-}$: Localized versus delocalized bonding in two isomeric intermetalloid clusters. *Chem. Eur. J.* **2018**, *24*, 699–705.

(32) Korber, N. The shape of germanium clusters to come. *Angew. Chem., Int. Ed.* **2009**, *48*, 3216–3217.

(33) Zhou, B.; Denning, M. S.; Kays, D. L.; Goicoechea, J. M. Synthesis and isolation of $[Fe@Ge_{10}]^{3-}$: A pentagonal prismatic Zintl ion cage encapsulating an interstitial iron atom. *J. Am. Chem. Soc.* **2009**, *131*, 2802–2803.

(34) Jin, X.; Espinoza-Quintero, G.; Below, B.; Arcisauskaite, V.; Goicoechea, J. M.; McGrady, J. E. Structure and bonding in a bimetallic endohedral cage, $[Co_2@Ge_{16}]^{z-}$. *J. Organomet. Chem.* **2015**, *792*, 149–153.

(35) Suchentrunk, C.; Korber, N. ${Ge_5}^{2-}$ Zintl anions: synthesis and crystal structures of $[K([2.2.2]crypt)]_2Ge_5 \cdot 4\,NH_3$ and $[Rb([2.2.2]crypt)]_2Ge_5 \cdot 4\,NH_3$. *New J. Chem.* **2006**, *30*, 1737–1739.

(36) Xia, Y. Iron-based Phenol-bridged imidazolium-containing Complexes: Synthesis, Characterization and Catalysis. Ph.D. thesis, 2012.

(37) Sheldrick, G. M. *SHELXT* – Integrated space-group and crystal-structure determination. *Acta Cryst. Section A* **2015**, *71*, 3–8.

(38) Dolomanov, O. V.; Bourhis, L. J.; Gildea, R. J.; Howard, J. A. K.; Puschmann, H. *OLEX2*: a complete structure solution, refinement and analysis program. *J. App. Cryst.* **2009**, *42*, 339–341.

(39) te Velde, G.; Bickelhaupt, F. M.; Baerends, E. J.; Fonseca Guerra, C.; van Gisbergen, S. J. A.; Snijders, J. G.; Ziegler, T. Chemistry with ADF. *J. Comput. Chem.* **2001**, *22*, 931–967.

(40) Van Lenthe, E.; Baerends, E. J. Optimized Slater-type basis sets for the elements 1–118. *J. of Comp. Chem.* **2003**, *24*, 1142–1156.

(41) Perdew, J. P.; Burke, K.; Ernzerhof, M. Generalized gradient approximation made simple. *Phys. Rev. Lett.* **1996**, *77*, 3865–3868.

(42) Fdez. Galván, I. et al. OpenMolcas: from source code to insight. *J. Chem. Theory and Computation* **2019**, *15*, 5925–5964.

(43) Aquilante, F. et al. Modern quantum chemistry with [Open]Molcas. *J. Chem. Phys.* **2020**, *152*, 214117.

(44) Pierloot, K.; Dumez, B.; Widmark, P.; Roos, B. Density-matrix averaged atomic natural orbital (ANO) basis sets for correlated molecular wave-functions. 4. Medium-size basis sets for the atoms H-Kr. *Theor. Chim. Acta* **1995**, *90*, 87–114.

(45) Hess, C. R.; Weyhermüller, T.; Bill, E.; Wieghardt, K. Fe(tim)$_2$: An Fe-Fe dimer containing an unsupported metal–metal bond and redox-active N4 macrocyclic ligands. *Angew. Chem., Int. Ed.* **2009**, *48*, 3703–3706.

(46) Bockman, T. M.; Cho, H.-C.; Kochi, J. K. Charge-transfer crystals of octacarbonyldiferrate. Solid-state structure and oxidation-reduction of an iron-iron-bonded electron donor. *Organometallics* **1995**, *14*, 5221–5231.

(47) Deng, H.; Shore, S. G. Crystal structure, infrared, and NMR spectra of tetrakis(pyridine-N) sodium octacarbonyldiiron $[(C_5H_5N)_4Na]_2[Fe_2(CO)_8]_\infty$: a two-dimensional extended structure due to sodium-isocarbonyl interactions. *Inorg. Chem.* **1992**, *31*, 2289–2291.

(48) Putnik, C. F.; Welter, J. J.; Stucky, G. D.; D'Aniello, M. J.; Sosinsky, B. A.; Kirner, J. F.; Muetterties, E. L. Metal clusters in catalysis. 15. A structural and chemical study of a dinuclear metal complex, hexacarbonylbis(η^3-2-propenyl)diiron(Fe-Fe). *J. Am. Chem. Soc.* **1978**, *100*, 4107–4116.

(49) Luart, D.; Sellin, M.; Laurent, P.; Salauen, J.-Y.; Pichon, R.; Toupet, L.; Des Abbayes, H. Synthesis and Crystal Structure of a New Binuclear Organoiron Nonbridged Complex: Bis(tert-butoxycarbonyl)octacarbonyldiiron, $[Fe(CO_2tBu)(CO)_4]_2$. *Organometallics* **1995**, *14*, 4989–4991.

(50) Pham, H. T.; Dang, C.-T. P.; Trung, N. T.; Ngan, V. T. Transformation between Hexagonal Prism and Antiprism of the Singly and Doubly Cr-Doped Ge_{12} Clusters. *J. Phys. Chem. A* **2019**, *123*, 10721–10729.

(51) Pham, H. T.; Majumdar, D.; Leszczynski, J.; Nguyen, M. T. 4d and 5d bimetal doped tubular silicon clusters $Si_{12}M_2$ with M = Nb, Ta, Mo and W: a bimetallic configuration model. *Phys. Chem. Chem. Phys.* **2017**, *19*, 3115–3124.

(52) Pham, H. T.; Phan, T.-T.; Tam, N. M.; Duong, L. V.; Pham-Ho, M. P.; Nguyen, M. T. Mn_2@Si_{15}: the smallest triple ring tubular silicon cluster. *Phys. Chem. Chem. Phys.* **2015**, *17*, 17566–17570.

(53) Huang, X.; Xu, H.-G.; Lu, S.; Su, Y.; King, R. B.; Zhao, J.; Zheng, W. Discovery of a silicon-based ferrimagnetic wheel structure in $V_xSi_{12}^-$ (x = 1–3) clusters: photoelectron spectroscopy and density functional theory investigation. *Nanoscale* **2014**, *6*, 14617–14621.

(54) Han, J.-G.; Zhao, R.-N.; Duan, Y. Geometries, stabilities, and growth patterns of the bimetal Mo_2-doped Si_n (n = 9–16) clusters: a density functional investigation. *J. Phys. Chem. A* **2007**, *111*, 2148–2155.

(55) Perdew, J. P.; Ernzerhof, M.; Burke, K. Rationale for mixing exact exchange with density functional approximations. *J. Chem. Phys.* **1996**, *105*, 9982–9985.

(56) Adamo, C.; Barone, V. Toward reliable density functional methods without adjustable parameters: The PBE0 model. *J. Chem. Phys.* **1999**, *110*, 6158–6170.

(57) Bader, R. F. W. A quantum theory of molecular structure and its applications. *Chem. Rev.* **1991**, *91*, 893–928.

(58) Outeiral, C.; Vincent, M. A.; Martín-Pendás, A.; Popelier, P. L. A. Revitalizing the

concept of bond order through delocalization measures in real space. *Chem. Sci.* **2018**, *9*, 5517–5529.

(59) Ghosh, S.; Cramer, C. J.; Truhlar, D. G.; Gagliardi, L. Generalized-active-space pair-density functional theory: an efficient method to study large, strongly correlated, conjugated systems. *Chem. Sci.* **2017**, *8*, 2741–2750.

(60) Vogiatzis, K. D.; Li Manni, G.; Stoneburner, S. J.; Ma, D.; Gagliardi, L. Systematic expansion of active spaces beyond the CASSCF limit: a GASSCF/SplitGAS benchmark study. *J. Chem. Theory and Computation* **2015**, *11*, 3010–3021.

(61) Ma, D.; Li Manni, G.; Gagliardi, L. The generalized active space concept in multiconfigurational self-consistent field methods. *J. Chem. Phys.* **2011**, *135*, 044128.

(62) Odoh, S. O.; Manni, G. L.; Carlson, R. K.; Truhlar, D. G.; Gagliardi, L. Separated-pair approximation and separated-pair pair-density functional theory. *Chem. Sci.* **2016**, *7*, 2399–2413.

(63) Roos, B.; Borin, A.; Gagliardi, L. Reaching the maximum multiplicity of the covalent chemical bond. *Angewandte Chemie International Edition* **2007**, *46*, 1469–1472.

Graphical TOC Entry

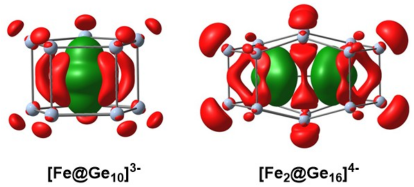

TOC Graphic.